Research Article Vol. 15, No. 7 / 1 Jul 2025 / Optical Materials Express 1407
Optical Materials EXPRESS

Effect of composition and two-step annealing on Ce-doped terbium iron garnets on Si

PANG-HSIAO LIU,[1,3] BIAZID KABIR MOGHAL,[2] AND BETHANIE J. H. STADLER[1,2,*]

[1]Department of Chemical Engineering and Materials Science, University of Minnesota, Minneapolis, 55454, Minnesota, USA
[2]Department of Electrical and Computer Engineering, University of Minnesota, Minneapolis, 55454, Minnesota, USA
[3]liu01908@umn.edu
[*]stadler@umn.edu

Abstract: Cerium-doped terbium iron garnet (CeTbIG) thin films with varying compositions and thicknesses were deposited to determine a garnet formation region. Both grain size and Faraday rotation (FR) increased in this region as the Ce content increased until 20% of the dodecahedral sites were occupied by Ce. The high Ce content was achieved by lowering the Fe ratio with respect to the total rare earth content. Above 20% Ce, the Faraday rotation was relatively independent of composition at -830°/cm, which is similar in magnitude to positive Faraday rotation garnets, e.g.: + 600°/cm for undoped TbIG. Next, we found that a two-step annealing method, involving a 400°C pre-anneal followed by higher temperatures, effectively reduced the maximum temperature from 900°C to 800°C without decreasing the Faraday rotation. Finally, a Si-integrated interferometer was simulated using the stable (+) and (-) Faraday rotation materials developed in this work. The simulation identified a Si-integrated Mach Zehnder Interferometers (MZI) with "push/pull" nonreciprocal phase shifts (NRPS) of opposite signs that enable mm-scale with zero external magnetic field (field-free).

© 2025 Optica Publishing Group under the terms of the Optica Open Access Publishing Agreement

1. Introduction

Optical isolators are essential components in optical systems such as telecommunications, laser systems, quantum photonics, and optical amplifiers, as they protect the gain medium of lasers from back-reflected light to mitigate instability of emitted signals. Ideal materials used in these devices are iron garnets (IGs) due to their non-reciprocal functionality [1–7]. In Si photonics, IG films are grown on silicon waveguides as top or side claddings through methods like sputter deposition or pulsed laser deposition (PLD) [8–13], enabling the propagating mode to interact with the magnetically saturated garnet film. For an optical isolator, when a magnetic field is transverse to the mode propagation direction, IG nonreciprocity causes nonreciprocal phase shift (NRPS). NRPS enables isolation when used in devices such as Mach Zehnder Interferometers (MZI) or ring resonators. However, when a magnetic field is parallel to the mode propagation direction, IG nonreciprocity causes nonreciprocal mode conversion (NRMC) for polarization orthogonality of reflections. Both phase shift and mode conversion devices can be simplified and have smaller footprints if both negative and positive gyrotropic materials are used [14–16].

The nonreciprocity of IG films, which depends on the off-diagonal terms in the permittivity tensor, can be characterized by measuring Faraday rotation [2,11]. Among IG materials, undoped and cerium-doped terbium iron garnets (CeTbIG) are particularly notable for their relatively high Faraday rotations and excellent compatibility with non-garnet substrates, such as silicon, without the need for seedlayers [17–19]. These advantages make TbIGs promising candidates for integration into optical isolators in silicon photonics.

#564014 https://doi.org/10.1364/OME.564014
Journal © 2025 Received 6 Apr 2025; revised 15 May 2025; accepted 15 May 2025; published 2 Jun 2025

Optical Materials EXPRESS

TbIG, with the nominal formula $Tb_3Fe_5O_{12}$, typically crystallizes in a cubic structure with a lattice parameter of approximately 1.2 nm and contains 8 formula units per unit cell. Tb cations nominally occupy 3 dodecahedral sites per formula unit, while Fe cations occupy 2 octahedral and 3 tetrahedral sites. When TbIG is doped with Ce cations, they substitute for Tb cations at the dodecahedral sites, resulting in the formula $(Ce,Tb)_3Fe_5O_{12}$ and enhanced Faraday rotation [18,19]. However, unlike its Faraday rotation-boosting counterpart bismuth, Ce cannot form pure iron garnet (CeIG) [2,11,20,21]. Therefore, the solubility limit of Ce in iron garnet needs to be considered to prevent the formation of CeO_2, which contributes weakly to the Faraday rotation in garnet films [21,22].

In practice, vacuum deposition involves multiple sources and mixed gases so variations in composition can occur while fabricating CeTbIG films. Reactive radiofrequency (RF) magnetron sputtering, equipped with two or more metal sources, is commonly used to grow uniform garnet films on large substrates. However, factors such as chamber environment (Ar/O_2 mixture ratio) and target erosion can impact the resulting characteristics of CeTbIG films in different batches, including phase formation, cation ratios, and deposition rates [23,24]. Therefore, in addition to the precise control of target bias voltages during the sputtering process to maintain the deposition rates of the desired ions, it is essential to thoroughly study CeTbIG films with varying compositions and thicknesses under consistent and controlled sputtering conditions. This approach aids in identifying a fabrication-tolerant region for garnet films. Key parameters, including grain size, magnetic properties, and Faraday rotation, are crucial in determining the suitability of CeTbIG films for practical applications.

In this work, we first investigated a series of annealed thin films on Si substrates, covering a wide range of stoichiometries and Ce doping levels. The composition of the thin films was characterized using scanning electron microscopy with energy-dispersive X-ray spectroscopy (SEM-EDS), and post-annealing phase formation was analyzed through X-ray diffraction (XRD) and electron backscatter diffraction (EBSD). The results revealed a phase diagram with a stable garnet formation region, with boundary conditions determined by the absence of the garnet phase and/or the presence of undesired phases. We then conducted a systematic study on how these variables influence grain size, magnetic properties, and Faraday rotation. Also, various thicknesses were considered to analyze the thickness effect on those parameters, providing clues to develop garnet claddings and also waveguides that may replace SiN waveguides (similar refractive index) for integrated photonic isolators [5,10]. We then applied a two-step annealing process, involving a 400°C pre-anneal followed by a high temperature annealing, to lower the maximum temperature required to obtain CeTbIG films on Si. Simulations were conducted using the measured values of nonreciprocity (gyrotropy) in order to estimate the footprint of Si-integrated MZI isolators and magnet free options are presented below.

2. Experiment results and discussion

2.1. Effect of composition on the formation of the garnet phase

A series of films with varying compositions and thicknesses were deposited on double-side polished silicon substrates using three elemental sources in a RF sputter deposition system. The compositions and thicknesses of the films were measured using SEM-EDS and a profilometer. To assess the effect of composition on garnet phase formation, we define two composition factors: R_1, the ratio of (Ce + Tb)/Fe, and R_2, the ratio of Ce/(Ce + Tb). R_1 indicates the deviation of a sample from the ideal cation stoichiometric ratio of 0.6 ((Ce + Tb)/Fe = 3/5), while R_2 indicates the proportion of Ce cations among the rare-earth cations. In this study, R_1 ranged from 0.4 to 1.0, R_2 from 0.0 to 4.0, and film thicknesses—150, 300, 500, and 700 nm—were controlled by adjusting the target bias voltage and deposition duration.

After deposition, the films were annealed at 900°C for 5 minutes using a rapid thermal annealer (RTA), which is a regular procedure for achieving high-quality TbIG films [17–19,25], and the

Optical Materials EXPRESS

resulting phases were determined by XRD. Figure 1(a) represents a phase diagram to summarize the region that exhibited single phase garnet (Fig. 1(b)), that is $R_2 < 0.20$ for $R_1 = 0.6$, $R_2 < 0.25$ for $R_1 = 0.7$, and $R_2 < 0.3$ for $R_1 = 0.8$. However, when R_1 was below 0.6 or exceeded 0.8, minor or major undesired oxide phases appeared in the films. This suggests that a fabrication-tolerant region for terbium iron garnet films exists, allowing for pure garnet formation even under a composition deviation due to the erosion or oxidation condition of metallic targets. Fig. S1(a) shows that thickness doesn't affect the garnet phase formation. Figure 1(c)-(d) shows the XRD patterns of thin films with excess Fe and Tb, respectively. The orange diamond patterns in Fig. 1(a) indicate regions undesired oxides in the films. The blue triangle patterns in Fig. 1(a) indicate regions with no garnet. Similarly, Fig. 1(e) shows the XRD pattern of a representative high Ce content film. It is worth noting that the solubility of Ce may vary depending on the deposition method, such as pulsed laser deposition and sol-gel method, and even with sputter deposition, garnet may exist outside the phase window, but not repeatably as seen in Fig. 1(a) [18,21].

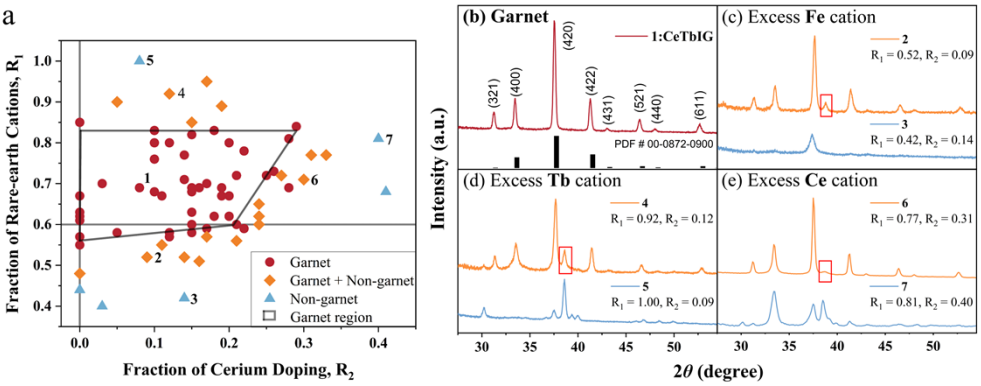

Fig. 1. (a) A scatter plot of phase formation for annealed films with various R_1 and R_2. Circle symbols (●) indicate that only the garnet phase was observed in the XRD patterns, diamond symbols (◆) indicate a mixture of garnet phase and minor non-garnet phase, and triangle symbols (▲) indicate a mixture of garnet phase and major non-garnet phase. (b-e) XRD patterns of (b) films within the fabrication-tolerant region, films with (c) excess Fe, (d) excess Tb, and (e) excess Ce. The orange patterns represent excess Fe ($0.45 < R_1 < 0.6$), Tb ($0.6 < R_1 < 0.9$), and Ce (slanted boundary of fabrication-tolerant region) causing the minor non-garnet phase formation, while the blue patterns represented more excess Fe ($R_1 < 0.45$), Tb ($R_1 > 0.9$), and Ce ($R_2 > 0.4$) causing major non-garnet phase formation. The red rectangles circle the obvious non-garnet peaks. All of the bars in (b) are from XRD PDF#00-0872-0900 for TbIG.

2.2. *Effect of composition on the grain size of the garnet films*

In addition to influencing phase formation, composition was also considered for its impact on the grain size of the garnet films. The films considered here were the garnet films in the fabrication-tolerance region, and categorized as $R_1 = 0.6$, 0.7 and 0.8. Grain size was assessed from SEM electron backscattering diffraction (EBSD) images and the TbIG and CeTbIG films exhibit fully crystallized grains with random crystalline orientation for all three R_1. As seen in Fig. 2(a), the mean grain size of the garnet films generally increased with an increase in R_2 while R_1 and thickness had no significant effect on grain size. (Fig. S1(b)) Although precise control over grain size was limited, Fig. 2(a) provides insights into the probable grain size range for fabricating garnet films with desired dimensions. For example, a CeTbIG film with a grain size

Optical Materials EXPRESS

of 4 μm or larger is most likely achieved with $R_2 > 0.2$. The largest mean grain size, 6.22 μm, was observed in a garnet film with $R_1 = 0.70$ and $R_2 = 0.25$, as shown in Fig. 2(b)-(c).

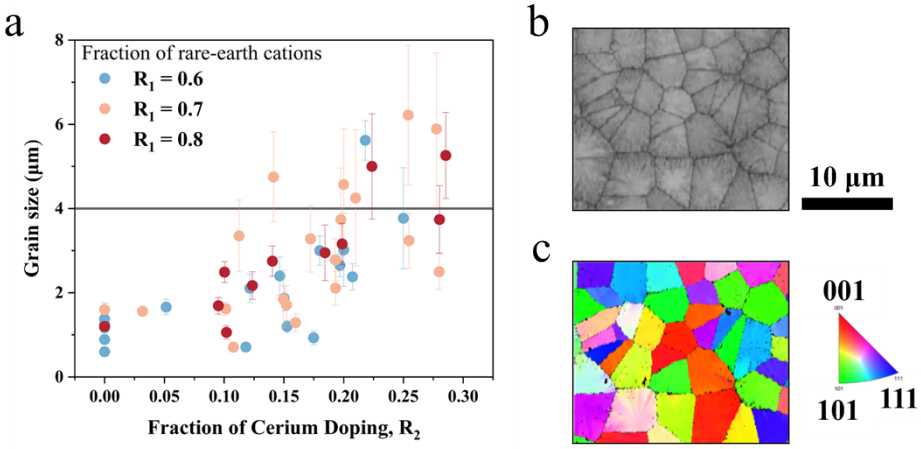

Fig. 2. (a) The plot of grain size as a function of R_1, R_2. (b-c) Electron backscatter diffraction (EBSD) map of the polycrystalline CeTbIG thin film on silicon with largest mean grain size of 6.22 μm. (b) The grayscale image represents the band contrast (top), and (c) the color image (bottom) is the inverse pole figure referenced to the z-direction of the crystal. The triangle is a guide to identify the polycrystalline cubic orientation. The scale bar for the images is 10 μm.

2.3. *Magnetic and magneto-optical characterization*

Room-temperature magnetic hysteresis measurements of the garnet films were conducted with both applied in-plane and out-of-plane magnetic fields using vibrating sample magnetometry (VSM). Since there is a difference of VSM sensitivity in the in-plane and out-of-plane geometries, the in-plane (IP) M_s was calibrated to match the out-of-plane (OOP) M_s for each film. Figure 3(a)-(b) showed the hysteresis loops for TbIG and CeTbIG film under IP and OOP measurement. The mean saturation magnetization, Ms, at room temperature of all the TbIG films was 10.1 ± 2.8 kA/m and that of all the CeTbIG films was 19.7 ± 5.9 kA/m, which is relatively small in the rare-earth IG family, such as YIG (~120-140 kA/m), EuIG (~90-100 kA/m), DyIG (~30 kA/m), and except gadolinium iron garnet (GdIG) on Si with M_s ~ 5-10 kA/m due to the compensation temperature being close to room temperature [9,11,20,22,26–30]. The ratio of the remnant magnetization to the saturation magnetization, M_r/M_s, was also extracted from hysteresis loops with IP and OOP magnetic field. CeTbIG films exhibited respective Mr/Ms ratio of 0.61 ± 0.04 for IP and 0.47 ± 0.08 for OOP, showing no obvious change from the values observed for TbIG films (0.62 ± 0.04 for IP and 0.45 ± 0.04 for OOP). Fortunately, IP M_r/M_s indicates high magnetization and therefore Faraday rotation after removing a magnetic field, which will enable the incorporation of garnet films in field-free photonic devices. Furthermore, both the coercivity and saturation field of the TbIG films were 0.9 ± 0.2 kOe and 5.1 ± 1.5 kOe, respectively, while those of the CeTbIG were 0.6 ± 0.2 kOe and 3.8 ± 1.2 kOe, respectively.

TbIG and CeTbIG films on Si substrates exhibit a preference for in-plane magnetic anisotropy (IMA) across various compositions, as observed from the hysteresis loops of the garnet films. To quantitatively describe IMA, the magnetic anisotropy energy (MAE) was calculated from the area difference between the anhysteretic loops up to the positive saturation field for the out-of-plane (OOP) and in-plane (IP) directions ($MAE = E_{OOP} - E_{IP}$) [19,20,28,30]. The anhysteretic loop is obtained by averaging the ascending and descending branches of the hysteresis loop. The

Optical Materials EXPRESS

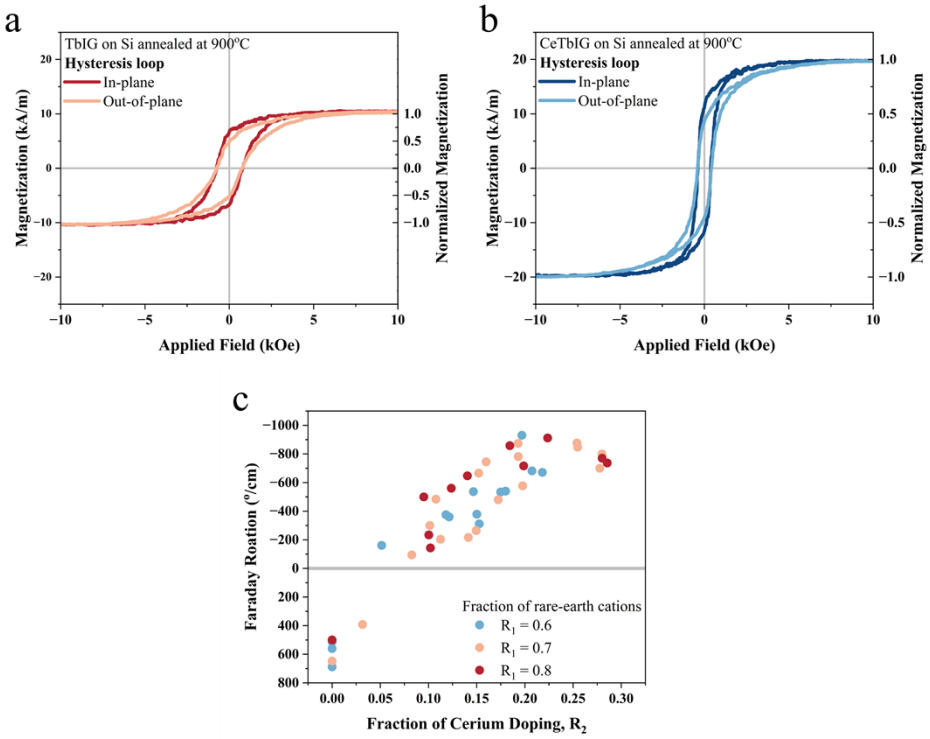

Fig. 3. (a-b) Room-temperature in-plane magnetic hysteresis measurement of the (a) TbIG film with $R_1 = 0.70$ and $R_2 = 0.00$ and (b) CeTbIG film with $R_1 = 0.61$ and $R_2 = 0.20$. (c) Faraday rotation of all the garnet films at 1550 nm as a function of R_1 and R_2.

respective MAE values of the TbIG and CeTbIG films were -0.86 ± 0.26 kJ/m^3 and -1.45 ± 0.57 kJ/m^3. The MAE can also be expressed as the sum of the growth-induced anisotropy (K_G), magnetoelastic anisotropy (K_{me}), shape anisotropy (K_{sh}), and magneto-crystalline anisotropy (K_{mc}). However, K_G and K_{mc} are negligible due to the weak crystallinity of the as-deposited garnet films and the polycrystalline nature of the post-annealed garnet films. Therefore, the MAE becomes

$$MAE = K_{me} + K_{sh} = K_{me} - \frac{\mu_0 M_s^2}{2} \quad (1)$$

Given that TbIG and CeTbIG films exhibit a weak shape anisotropy ($\mu_0 M_s^2/2 = \sim 0.064$ and ~ 0.24 kJ/m^3), the MAE is primarily dominated by the K_{me} term in all the garnet films. This dominance suggests that a stronger K_{me} supports the remnant in-plane magnetization for garnet films on Si which will be needed for latched non-reciprocal waveguide isolators. Combining the high IP M_r/M_s values, the IMA nature of the TbIG and CeTbIG films enables their use as cladding on Si waveguides in field-free optical isolators.

Room temperature Faraday rotation measurements were performed on all films out of plane using a wavelength of 1550 nm and a magnetic field of ±3kOe, Fig. 3(c). The Faraday rotation of TbIG films was +600 ± 100°/cm and was relatively independent of R_1, while the sign changed due to the negative contribution from Ce doping. The Faraday rotation of CeTbIG films increased as the Ce content increased and reached -830 ± 100°/cm when $R_2 > 0.2$. A composition with higher Faraday rotation of -930°/cm at $R_1 = 0.61$ and $R_2 = 0.20$ and was used to investigate the effect of the two-step annealing.

Optical Materials EXPRESS

2.4. Two-step annealing

Based on previous work, two-step annealing was next conducted, involving a 400°C anneal for 5 minutes to form nuclei, followed by a higher regular treatment ranging from 800°C to 950°C for 5 minutes [31]. Figure 4(a) shows the XRD patterns of the CeTbIG films on Si that were as-deposited, annealed at 400°C, and annealed at 900°C. As reported previously, as-deposited CeTbIG requires at least 800°C to form the pure garnet phase [10,20]. After a series of one-step and two-step annealing processes, the desired garnet peaks were obtained, but small quantities of CeO_2 appeared in the garnet film at 950°C, marked and shown in Fig. 4(b)-(c). CeO_2 phase, a stable thermodynamic oxide, doesn't contribute magnetic moment and often forms in TbIG film incorporated with high Ce content or annealed at higher temperature [18,21]. Figure 4(d)-(k) show the SEM EBSD images of the one-step and two-step annealed CeTbIG films on Si with grain sizes of about 2.2-2.6 μm, indicating that the annealing did not changed the grain size appreciably. It is worth noting that although the peaks of the oxide phase were small compared to the large garnet peak in the XRD pattern, the large black background represented 31% of the sample was occupied by the oxide phase in the EBSD image.

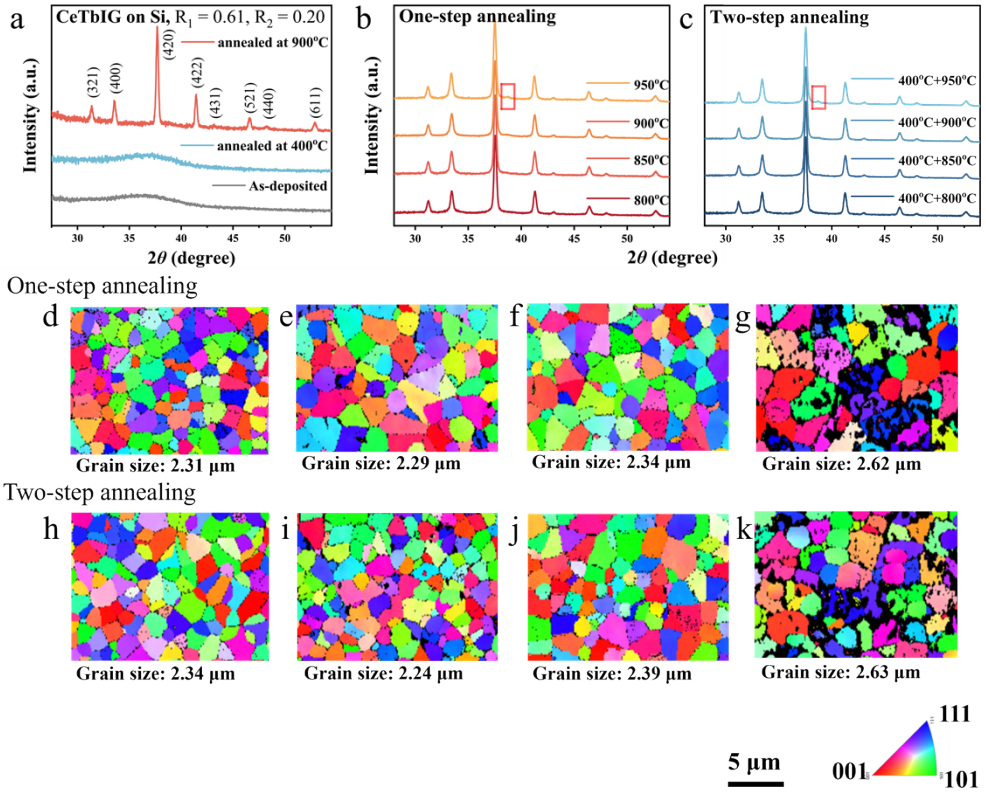

Fig. 4. (a) XRD patterns of an as-deposited CeTbIG, CeTbIG annealed at 400°C, and CeTbIG annealed at 900°C. XRD patterns of (b-c) XRD patterns of the CeTbIG after (b) the one-step annealing (800°C-950°C) and (c) the two-step annealing (400°C + 800°C-950°C). (d) SEM EBSD images of the CeTbIG . The average grain sizes were analyzed by the software after the images were collected. The color image is the inverse pole figure referenced to the z-direction of the crystal. The orientation triangle is a guide to identify the cubic orientation. The scale bar for the images is 5 μm.

Optical Materials EXPRESS

Figure 5(a)-(b) shows IP magnetic hysteresis loops at room temperature for CeTbIG on Si after one-step and two-step annealing. For one-step annealing, the area within hysteresis loop became slightly larger as temperature decreased. In contrast, for two-step annealing, the area was relatively independent of temperature, indicating that the two-step annealing reduced the difference of saturation field between the CeTbIG on Si being annealed at different temperatures. In both one-step and two-step annealing, the magnetization of garnet films annealed at 950°C was slightly decreased due to the non-garnet phase. A similar phenomenon was observed in the OOP magnetic hysteresis loops shown in Fig. S2.

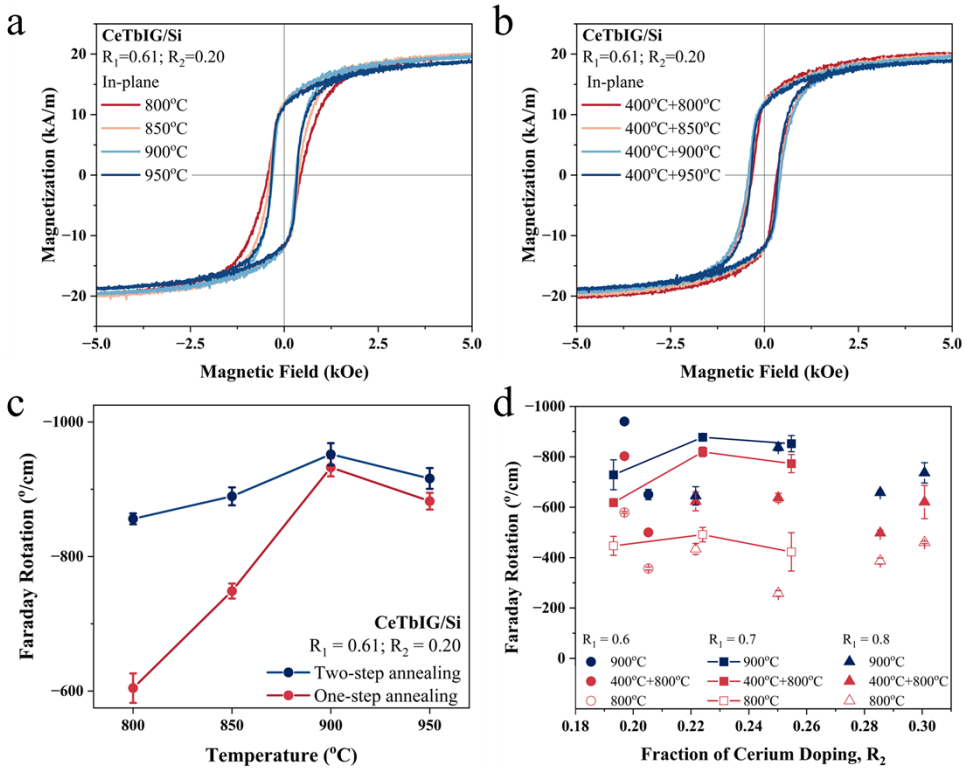

Fig. 5. (a,b) Room-temperature in-plane magnetic hysteresis measurement of the CeTbIG films after a) the one-step annealing and (b) the two-step annealing. Faraday rotation measurements in transmission at 1500 nm wavelength and ±3kOe field for (c) the CeTbIG with $R_1 = 0.61$ and $R_2 = 0.20$ after one-step and two-step annealing and for (d) the CeTbIG with three different R_1 and high R_2.

The Faraday rotation of the CeTbIG films after one-step and two-step annealing were measured OOP using a wavelength of 1550 nm and a magnetic field of ±3kOe. Figure 5(c) shows the comparison of the Faraday rotation of the CeTbIG on Si after the two processes. For one-step annealing, Faraday rotation of the CeTbIG film had the largest value of -930°/cm at 900°C and dropped to -600°/cm at 800°C, indicating that Faraday rotation was sensitive to annealing temperature in this range. Differently, for two-step annealing, the largest Faraday rotation was -950°/cm at 400°C + 900°C and -860°/cm at 400°C + 800°C, indicating that the two-step annealing indeed improved Faraday rotation while being less sensitive to thermal processing than one-step annealing. For both one-step and two-step annealing, Faraday rotation of the garnet films annealed at 950°C decreases might be due to the presence of the non-garnet phase. Furthermore, Fig. 5(d) shows the effect of the two-step annealing on Faraday rotation of the

Optical Materials EXPRESS

garnet films with high cerium content ($R_2 > 2.0$ for each R_1). Faraday rotation of those garnet films anneal at 400°C + 800°C were improved at least one third compared to those annealed at 800°C and yet all values are within a magnitude that enables balanced devices with push-pull gyrotropies involving positive Faraday rotators, such as undoped TbIG reported here.

2.5. NRPS calculations and isolator design

Nonreciprocal phase shift (NRPS) was simulated for Si waveguides with claddings of the materials developed above in order to estimate footprints that would be needed in future Si-integrated isolators. NRPS was first proposed by Yamamoto and Makimoto in 1974 and estimated by calculating the difference between the forward and backward propagation constants ($\beta_{forward} - \beta_{backward}$) of garnet claddings on silicon-on-insulator (SOI) waveguides [32,33]. Here, simulations were performed using refractive indices and Faraday rotations (θ_F) at wavelength of 1550 nm ($n_{TbIG} = 2.1$, $n_{CeTbIG} = 2.2$ [16,34]; $\theta_{F,TbIG} = +600°/cm$, $\theta_{F,CeTbIG} = -830°/cm$). The Si waveguides were 220 nm thick and 500 nm wide, as these dimensions are typical for integrated Si photonics. The NRPS increased with garnet thickness up to 400 nm, after which the calculated NRPS values were constant at -660 rad/m (-380°/cm) for TbIG and +910 rad/m (+520°/cm) for CeTbIG, respectively. (calculation results are shown in Fig. S3) The sign of NRPS is determined by how the mode profile overlaps with the magneto-optical perturbation. In single mode waveguides with garnet top claddings, a positive Faraday rotation leads to a net reduction in the propagation constant for the forward mode compared to the backward mode, and vice versa [35].

The first Mach–Zehnder interferometer (MZI) isolator was proposed by Auracher and Witte in 1975 and garnet-based MZI-isolator began development in 1986 and continued to evolve in the following years [36–39]. An MZI isolator is made of two branches with a π/2 reciprocal phase shifter (RPS) in one branch and π/2 non-reciprocal phase shifter(s) in various configurations shown below [2,4,36]. The latter are TbIG- or CeTbIG- cladded Si as shown in Fig. 6 below. Non-reciprocal phase shifter will change the sign of the phase shift depending on the light propagation direction. For effective isolation, the difference in total phase shift between the branches must be 0 (constructive) in the forward direction and π (destructive) in the backward direction.

For an MZI isolator with one non-reciprocal branch, destructive interference of reflected light will require TbIG or CeTbIG cladded lengths of 2.38 mm or 1.73 mm, respectively. (Figure 6(a)) The constructive and destructive interference occurs due to a phase difference (Δφ) between the branches of the MZI. In Fig. 6(a), this will mean designing the bottom branch to have a length of 2mπ, where m is an integer, and the top branch to have this length plus an extra quarter wavelength ($l_{RPS} = \lambda/4/n_{eff} \sim 200$ nm) or longer ($l_{RPS} = \lambda/4/n_{eff} + 2n\pi$), where n_{eff} is an effective refractive index and n is an integer.

$$\Delta\varphi = \varphi_{top} = \frac{\pi}{2} + \left(-\frac{\pi}{2}\right) = 0 \quad [forward] \tag{2}$$

$$\Delta\varphi = \varphi_{top} = \frac{\pi}{2} + \left(+\frac{\pi}{2}\right) = \pi \quad [backward] \tag{3}$$

To reduce the total interferometer length while maintaining unidirectional magnetization, a push-pull interferometer with CeTbIG and TbIG in the two branches will halve the required garnet-clad lengths to 0.865 mm on the top branch and 1.19 mm on the bottom branch (Fig. 6(b)). In Fig. 6(b), this will mean designing one branch to be l_{RPS} longer than the other, so the phase difference between the branches is:

$$\Delta\varphi = \left(\frac{\pi}{2} + \left(-\frac{\pi}{4}\right)\right)_{top} - \left(+\frac{\pi}{4}\right)_{bottom} = 0 \quad [forward] \tag{4}$$

$$\Delta\varphi = \left(\frac{\pi}{2} + \left(+\frac{\pi}{4}\right)\right)_{top} - \left(-\frac{\pi}{4}\right)_{bottom} = \pi \quad [backward] \tag{5}$$

Optical Materials EXPRESS

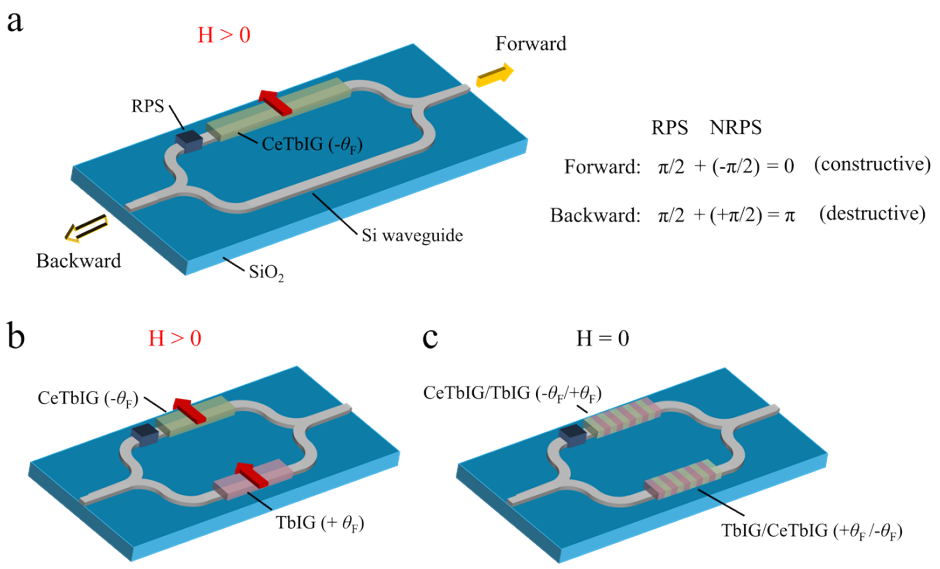

Fig. 6. Schematics of MZI isolator with (a) one nonreciprocal branch of CeTbIG ($-\theta_F$) thin film, (b) two nonreciprocal branches of respective CeTbIG ($-\theta_F$) and TbIG ($+\theta_F$) thin film, and (c) two branches of alternative CeTbIG and TbIG segment thin films. Both (a) and (b) require an external unidirectional magnetic field ($H > 0$), whereas (c) operates without a fixed magnetic field ($H = 0$). The required length of the garnet cladding can be calculated by dividing the required shift ($\pi/2$ for one branch and $\pi/4$ for two branches) by the NRPS of the garnet material. Reciprocal phase shifters (RPSs) are included to ensure constructive interference in the forward direction and destructive interference in the backward direction.

However, external magnets would be necessary to enforce this unidirectional transverse magnetization; otherwise, the garnet shape anisotropy would dominate along the light propagation direction. This direction favors nonreciprocal mode conversion (NRMC) devices [10] if magnet-free applications are desired. Alternatively, for a magnet-free MZI isolator, potential claddings could be engineered with alternating garnet segments having opposite nonreciprocity [40]. Dipole coupling would maintain opposing magnetic orientations due to their low-energy configuration and large IP remnant magnetization, accumulating the phase shift suitable for an NRPS isolator. (Figure 6(c))

3. Conclusion

Garnet thin films with varying Tb and Ce content and thickness were deposited on Si substrates by RF sputtering deposition to find a fabrication-tolerant region. This systematic study revealed the relationship between the above-mentioned variables and grain size, magnetic properties, and Faraday rotation. The grain size generally increased as the Ce content increased and the largest mean grain size (6.22 μm) was obtained at $R_1 = 0.70$ and $R_2 = 0.25$. Additionally, the M_r/M_s values were about 0.60 for all the garnet films by in-plane room-temperature magnetic hysteresis measurement, which is suitable for developing a field-free isolator in tiny and complicated photonic devices. Importantly, we found CeTbIG thin film on Si with $R_2 > 0.2$ has stable Faraday rotation values for a fabrication-tolerant region at high Ce doping. Furthermore, the two-step annealing, involving a low temperature pre-anneal followed by a high temperature treatment, reduced the temperature dependence of the saturation magnetization extracted from hysteresis loops. This offers an effective method to lower the maximum annealing temperature from 900°C

Optical Materials EXPRESS

to 800°C. Incorporating a first anneal of 400°C increased Faraday rotation of films with different R_1 and high Ce content annealed at 800°C by one third while keeping the magnitude of these negative gyrotropies within range of positive gyrotropy materials for push/pull isolator designs. Simulations were conducted to estimate the nonreciprocal phase shift enabled by coating SOI waveguides with the garnets developed in this study, and several isolator designs were proposed that are mm-scale and an example without external magnetic fields.

4. Methods

4.1. Fabrication of TbIG and CeTbIG films

Thin films of TbIG and CeTbIG were sputter deposited using RF magnetron co-sputtering in a reactive argon and oxygen ambient (10:1) on 10 mm × 10 mm Si (100) substrates at a base pressure of 1.5-1.7 mTorr. Three independently controlled sputtering sources were used to control the individual sputter rates for compositions of $R_1 = 0.40$-1.00 and $R_2 = 0.00$-0.40. Annealing processes were done by SOLARIS 150 rapid thermal processing system or rapid thermal annealer (RTA). For one-step annealing, the garnet films were annealed in RTA at 900°C for 5 min in 1 SLM of O_2, while for two-step annealing, the garnet films were preheated in an RTA at 400°C for 5 min in 1 SLM of O_2 and then the temperature was increased to 800°C-950°C for 5 min also in 1 SLM of O_2.

4.2. Structural and Elemental Characterization

The thicknesses of the films were measured using a KLA Tencor P-16 surface profilometer. The structural X-ray patterns were recorded on a Bruker D8 Discover 2D diffractometer from a θ–2θ scan, which has a Co (K_α) source of wavelength 1.789 Å. The polycrystalline peaks were identified with a database reference (PDF #00-0872-0900) corresponding to cubic terbium iron garnet using MDI JADE. Crystallite size analysis and elemental composition was determined using Oxford electron backscattering diffraction (EBSD) and electron dispersive spectroscopy (EDS) detector in a ThermoFisher Apreo 2S scanning electron microscope (SEM), respectively.

4.3. Magnetic and Magneto-optical Measurements

The room temperature hysteresis measurements were collected on a Princeton Measurements micro-vibrating sample magnetometer (μVSM) and the field was swept between +10 kOe and −10 kOe. The specimen (on an adhesive tape) was mounted on a sample rod, and the background subtraction was carried out in Origin Pro 2024b. Thin layers with a low magnetic moment are particularly difficult to measure, so the VSM was calibrated with a 10 mm x10 mm sample of pure Alfa Ni film (Weight: 595.7 ± 20 mg, Thick: 0.006 mm, and Purity: 99.95%) on a 10 mm x10 mm DSP Si substrate. The VSM was calibrated also before each measurement orientation using this Ni foil through which highly accurate saturation magnetization was obtained for our thin films. The magnetic anisotropy energy from magnetometry was obtained from the difference in the area under the anhysteretic M–H curves for the in-plane and out-of-plane geometries. Faraday rotation measurements were recorded in transmission setup using a laser wavelength of 1550 nm and a magnetic field of ±3kOe.

4.4. NRPS calculations

The NRPS of waveguide devices were calculated using Lumerical Finite-Difference Eigenmode (FDE) solver. For the NRPS calculation, the device structure was constructed with a Si waveguide layer, a magneto-optical upper cladding layer, and a silicon oxide substrate. Fundamental TM mode was considered as the propagating light in the structure under a magnetic field perpendicular to light propagation. The optical properties of TbIG and CeTbIG utilized include the dielectric

Optical Materials EXPRESS

permittivity tensors, ε_{TbIG} and ε_{CeTbIG},

$$\varepsilon_{TbIG\ or\ CeTbIG} = \begin{bmatrix} \varepsilon_{xx} & 0 & 0 \\ 0 & \varepsilon_{yy} & +i\gamma_{xy} \\ 0 & -i\gamma_{xy} & \varepsilon_{zz} \end{bmatrix} \quad (6)$$

where $\varepsilon_{xx} = \varepsilon_{yy} = \varepsilon_{zz} = n^2_{\mathrm{TbIGor}CeYIG}$, and γ is the off-diagonal term of the dielectric constant tensor, which is determined by the refractive index and Faraday rotation (θ_F) at a wavelength of 1550 nm, as $2n_{garnet}\ \theta_F/k_0$, where k_0 is the wavenumber in vacuum. To calculate effective refraction indices of the structure, Si ($n_{Si} = 3.45$) and SiO_2 ($n_{SiO2} = 1.46$) were used for the waveguide and substrate material.

The most important part of the simulation is the insertion of anisotropic magneto-optical effect in the waveguide structure, which is followed by multiplying a unitary matrix U and its complex conjugate transpose U* with the permittivity tensors ε_{TbIG} and ε_{CeTbIG}, respectively [32]. A matrix transformation grid attribute is also created based on this U matrix which needs to be defined and added in the magneto-optical material parameter settings to achieve the magneto-optical effect. Finally, the propagation constant values will be different in the forward and backward magnetic field directions due to the inserted magneto-optical effect in the waveguide. This difference will provide us with the required NRPS values.

Funding. National Science Foundation; National Science and Technology Infrastructure Program (ECCS-2025124); Magnetic measurements were conducted at the Institute of Rock Magnetism (IRM) (EAR 2153786).

Acknowledgments. Portions of this work were conducted in the Characterization Facility and Minnesota Nano Center, which are supported by the National Science Foundation (NSF) through the National Nanotechnology Coordinated Infrastructure (NNCI) under Award Number ECCS-2025124. Magnetic measurements were conducted at the Institute of Rock Magnetism (IRM) supported via NSF, Earth Science Division under EAR 2153786

Disclosures. The authors declare that there are no conflicts of interest related to this article.

Data availability. Data underlying the results presented in this paper are not publicly available at this time but may be obtained from the authors upon reasonable request.

Supplemental document. See Supplement 1 for supporting content.

References

1. D. Jalas, A. Petrov, M. Eich, *et al.*, "What is — and what is not — an optical isolator," Nat. Photonics **7**(8), 579–582 (2013).
2. K. Srinivasan and B. J. H. Stadler, "Review of integrated magneto-optical isolators with rare-earth iron garnets for polarization diverse and magnet-free isolation in silicon photonics [Invited]," Opt. Mater. Express **12**(2), 697–716 (2022).
3. Q. Du, T. Fakhrul, Y. Zhang, *et al.*, "Monolithic magneto-optical oxide thin films for on-chip optical isolation," MRS Bull. **43**(6), 413–418 (2018).
4. Y. Shoji and T. Mizumoto, "Magneto-optical non-reciprocal devices in silicon photonics," Sci. Technol. Adv. Mater. **15**(1), 014602 (2014).
5. J. Lapointe, C. Coia, A. Dupont, *et al.*, "Passive broadband Faraday isolator for hybrid integration to photonic circuits without lens and external magnet," Nat. Photonics **19**(3), 248–257 (2025).
6. S.-Y. Ren, W. Yan, L.-T. Feng, *et al.*, "Single-Photon Nonreciprocity with an Integrated Magneto-Optical Isolator," Laser Photonics Rev. **16**(5), 2100595 (2022).
7. K. Saker, M. Lahoubi, and S. Pu, "Optimized magneto-optical isolator design based on cerium-substituted yttrium iron garnet fiber," Opt. Quant. Electron. **53**(6), 334 (2021).
8. L. Bi, J. Hu, P. Jiang, *et al.*, "On-chip optical isolation in monolithically integrated non-reciprocal optical resonators," Nat. Photonics **5**(12), 758–762 (2011).
9. Y. Zhang, Q. Du, C. Wang, *et al.*, "Dysprosium substituted Ce:YIG thin films with perpendicular magnetic anisotropy for silicon integrated optical isolator applications," APL Mater. **7**(8), 081119 (2019).
10. K. Srinivasan, C. Zhang, P. Dulal, *et al.*, "High-Gyrotropy Seedlayer-Free Ce:TbIG for Monolithic Laser-Matched SOI Optical Isolators," ACS Photonics **6**(10), 2455–2461 (2019).
11. T. Fakhrul, S. Tazlaru, L. Beran, *et al.*, "Magneto-Optical Bi:YIG Films with High Figure of Merit for Nonreciprocal Photonics," Adv. Opt. Mater. **7**(13), 1900056 (2019).

Optical Materials EXPRESS

12. G. Portela, M. Levy, and H. E. Hernandez-Figueroa, "Novel compact magnetless isolator based on a magneto-optical garnet material," Opt. Laser Technol. **157**, 108638 (2023).
13. D. Minemura, R. Kou, Y. Sutoh, *et al.*, "Compact magneto-optical isolator by μ-transfer printing of magneto-optical single-crystal film on silicon waveguides," Opt. Express **31**(17), 27821–27829 (2023).
14. H. Yokoi, T. Mizumoto, N. Shinjo, *et al.*, "Demonstration of an optical isolator with a semiconductor guiding layer that was obtained by use of a nonreciprocal phase shift," Appl. Opt. **39**(33), 6158–6164 (2000).
15. R. Wolfe, J. Hegarty, J. Dillon, *et al.*, "Magneto-optic waveguide isolators based on laser annealed (Bi, Ga) YIG films," IEEE Trans. Magn. **21**(5), 1647–1650 (1985).
16. P. Dulal, A. D. Block, T. E. Gage, *et al.*, "Optimized Magneto-optical Isolator Designs Inspired by Seedlayer-Free Terbium Iron Garnets with Opposite Chirality," ACS Photonics **3**(10), 1818–1825 (2016).
17. P. Dulal, T. E. Gage, A. D. Block, *et al.*, "Sputter-deposited seedlayer-free cerium-doped terbium iron garnets for SOI waveguide isolators," in *2016 IEEE Photonics Conference (IPC)* (2016), pp. 773–774.
18. T. Fakhrul, S. Tazlaru, B. Khurana, *et al.*, "High Figure of Merit Magneto-Optical Ce- and Bi-Substituted Terbium Iron Garnet Films Integrated on Si," Adv. Opt. Mater. **9**(16), 2100512 (2021).
19. K. Srinivasan, C. Radu, D. Bilardello, *et al.*, "Interfacial and Bulk Magnetic Properties of Stoichiometric Cerium Doped Terbium Iron Garnet Polycrystalline Thin Films," Adv. Funct. Materials **30**(15), 2000409 (2020).
20. K. Hayashi, K. P. Dao, M. J. Gross, *et al.*, "Magneto-Optical Bi-Substituted Yttrium and Terbium Iron Garnets for On-Chip Crystallization via Microheaters," Adv. Opt. Mater. **12**(25), 2400708 (2024).
21. H. Shen, H. Wang, J. Ma, *et al.*, "Modulation of structure and magnetic properties of terbium iron garnet by the introduction of Bi3+ and Ce3+," J. Sol-Gel Sci. Technol. **103**(2), 539–548 (2022).
22. M. Huang and S.-Y. Zhang, "Growth and characterization of cerium-substituted yttrium iron garnet single crystals for magneto-optical applications," Appl. Phys. A: Mater. Sci. Process. **74**(2), 177–180 (2002).
23. Y. Abe, M. Kawamura, and K. Sasaki, "Effects of oxygen gettering and target mode change in the formation process of reactively sputtered Pt oxide thin films," J. Vac. Sci. Technol., A **18**(5), 2608–2612 (2000).
24. N. D. Madsen, B. H. Christensen, S. Louring, *et al.*, "Controlling the deposition rate during target erosion in reactive pulsed DC magnetron sputter deposition of alumina," Surf. Coat. Technol. **206**(23), 4850–4854 (2012).
25. S. Damerio and C. O. Avci, "Sputtered terbium iron garnet films with perpendicular magnetic anisotropy for spintronic applications," J. Appl. Phys. **133**(7), 073902 (2023).
26. K. Srinivasan, A. J. Grutter, T. E. Gage, *et al.*, "Interfacial magnetic characteristics of nearly compensated gadolinium iron garnet," Phys. Rev. Mater. **8**(4), 044403 (2024).
27. J. J. Bauer, E. R. Rosenberg, and C. A. Ross, "Perpendicular magnetic anisotropy and spin mixing conductance in polycrystalline europium iron garnet thin films," Appl. Phys. Lett. **114**(5), 052403 (2019).
28. E. R. Rosenberg, K. Litzius, J. M. Shaw, *et al.*, "Magnetic Properties and Growth-Induced Anisotropy in Yttrium Thulium Iron Garnet Thin Films," Adv. Electron. Mater. **7**(10), 2100452 (2021).
29. S. Mokarian Zanjani and M. C. Onbaşlı, "Predicting new iron garnet thin films with perpendicular magnetic anisotropy," J. Magn. Magn. Mater. **499**, 166108 (2020).
30. A. C. Kaczmarek, E. R. Rosenberg, Y. Song, *et al.*, "Atomic order of rare earth ions in a complex oxide: a path to magnetotaxial anisotropy," Nat. Commun. **15**(1), 5083 (2024).
31. T. E. Gage, P. Dulal, P. A. Solheid, *et al.*, "Si-integrated ultrathin films of phase-pure Y3Fe5O12 (YIG) via novel two-step rapid thermal anneal," Mater. Res. Lett. **5**(6), 379–385 (2017).
32. M. Li, Y. Zhao, S. Dai, *et al.*, "Compact and low loss magneto-optical waveguide isolator for TE mode based on lithium niobate on insulator," Opt. Commun. **495**, 127088 (2021).
33. S. Yamamoto and T. Makimoto, "Circuit theory for a class of anisotropic and gyrotropic thin-film optical waveguides and design of nonreciprocal devices for integrated optics," J. Appl. Phys. **45**(2), 882–888 (1974).
34. B. J. H. Stadler and T. Mizumoto, "Integrated Magneto-Optical Materials and Isolators: A Review," IEEE Photonics J. **6**(1), 1–15 (2014).
35. K. Shui, L. Nie, Y. Zhang, *et al.*, "Design of a compact waveguide optical isolator based on multimode interferometers using magneto-optical oxide thin films grown on silicon-on-insulator substrates," Opt. Express **24**(12), 12856–12867 (2016).
36. F. Auracher and H. H. Witte, "A new design for an integrated optical isolator," Opt. Commun. **13**(4), 435–438 (1975).
37. T. Mizumoto and Y. Naito, "Nonreciprocal Propagation Characteristics of YIG Thin Film," IEEE Trans. Microwave Theory Tech. **30**(6), 922–925 (1982).
38. T. Mizumoto, K. Oochi, T. Harada, *et al.*, "Measurement of optical nonreciprocal phase shift in a bi-substituted Gd3Fe5O12film and application to waveguide-type optical circulator," J. Lightwave Technol. **4**(3), 347–352 (1986).
39. Y. Okamura, T. Negami, and S. Yamamoto, "Integrated optical isolator and circulator using nonreciprocal phase shifters: a proposal," Appl. Opt. **23**(11), 1886–1889 (1984).
40. K. Srinivasan and B. J. H. Stadler, "Push-pull non-reciprocal phase shifting," United States patent US12055756B2 (August 6, 2024).